Materials Today Advances 16 (2022) 100293

Contents lists available at ScienceDirect

Materials Today Advances

journal homepage: www.journals.elsevier.com/materials-today-advances/

A physics-oriented memristor model with the coexistence of NDR effect and RS memory behavior for bio-inspired computing

X. Ji [a], Z. Dong [a, b, *], C.S. Lai [c, d], G. Zhou [e], D. Qi [a, **]

[a] College of Electrical Engineering, Zhejiang University, Hangzhou, 310027, China
[b] College of Electronic Information, Hangzhou Dianzi University, Hangzhou, 310018, China
[c] Department of Electronic and Electrical Engineering, Brunel University London, UB8 3PH, London, UK
[d] Department of Electrical Engineering, School of Automation, Guangdong University of Technology, Guangzhou 510006, China
[e] College of Artificial Intelligence, Southwest University, Chongqing, 400715, China

ARTICLE INFO

Article history:
Received 15 July 2022
Received in revised form
30 August 2022
Accepted 5 September 2022
Available online xxx

Keywords:
Negative differential resistance
Resistive switching
Memristor
Affective associative learning
Bio-inspired computing

ABSTRACT

Bio-inspired computing promises fundamentally different ways to advances in artificial intelligence with extreme energy efficiency. Memristive technologies due to the non-volatility, high density, low-power, and synaptic bionic properties can help in realizing bio-inspired architecture and its hardware implementation. This paper proposes a novel physics-oriented memristor model with coexistence of negative differential resistance (NDR) effect and resistive switching (RS) memory behavior for bio-inspired computing. Firstly, an Ag/TiO_x/FTO memristor is fabricated using sol-gel and magnetron sputtering method, and its performance test demonstrates that the coexistence of NDR effect and RS memory behavior can be modulated by the moisture. Then, a physical-oriented memristor model is constructed, which provides the possibility to explore the dynamics of the coexistence of NDR effect and RS memory behavior in simulation. Furthermore, a memristor-based affective computing circuit emulating the process of human affective associative learning is designed. The experiment demonstrates that the coexistence of NDR effect and RS memory behavior can change the memory time without additional circuit and cost, which is expected to realize the automatic conversion from short-term memory to long-term memory in bio-inspired computing.

1. Introduction

The bio-inspired computing system is a very-large-scale integrated circuit that uses dynamic and static circuits to mimic the neurobiological structure and function of the biological brain [1–4]. This system offers the potential to overcome imminent problems of the von Neumann computer architecture, particularly energy efficiency, device reliability, and software complexity [5–7]. Many studies have pointed out that brain intelligence research inspired by neuroscience can promote the development of a new generation of artificial intelligence technology and information industry [8–10].

Memristors are two-terminal electronic devices that exhibit resistive switching (RS), non-volatility, high density, low-power consumption, synaptic bionic, and have potential applications in the field of bio-inspired computing [11]. Especially, the coexistence of physical effect and RS memory behavior achieves a high-level simulation of the biomimetic or neuromorphic computing, which has been widely studied by researchers [12–16]. The coupling between capacitance and RS memory behavior was employed to implement the Hebbian-like learning in Ref. [12]. In Ref. [13], researchers fabricated an environment friendly memristor with coexistence of digital and analog switching properties, which was expected to achieve the realization of green-electronics and bio-inspired systems. The coexistence of negative differential resistance (NDR) effect and RS memory behavior observed in the NbO_x-based memristor could perform Boolean operations and be the third-order nanocircuit elements for bio-inspired computing engineering [14]. The prepared memristor exhibited the coexistence of negative photoconductance effect (NPC) and RS memory behavior, which could be used as a reconfigurable neuromorphic vision sensor and make the bio-inspired computing system more efficiency [15,16].

* Corresponding author. College of Electrical Engineering, Zhejiang University, Hangzhou, 310027, China.
** Corresponding author.
E-mail addresses: englishp@126.com (Z. Dong), qidl@zju.edu.cn (D. Qi).

https://doi.org/10.1016/j.mtadv.2022.100293

The memristor models aim to correlate the electrical properties with the underlying physical mechanisms [17]. Researchers presented a linear ion-drift model for a memristive device [18]. On this basis, in Ref. [19], a non-linear model with different window functions was constructed, which alleviated the bounds issue. Simmons proposed a memristor model based on the quantum tunnelling effect [20]. However, this model is complex as it does not consider an explicit relationship between current and voltage. The threshold adaptive memristor (TEAM) model has become renowned for its simplicity, generality, accuracy, and low computational complexity [21]. Reference [22] presented the voltage threshold adaptive memristor (VTEAM) model, which extends the TEAM model to describe the behavior of voltage-controlled memristors. The above-mentioned memristor models seldom consider the physical phenomena including the coexistence of physical effect and RS memory behavior. Recently, most of the studies have verified the coexistence of physical effect and RS memory behavior in material-level and analyzed the physical mechanism of the coexistence by piecewise linear fitting [12–16]. Meanwhile, the coexistence of physical effect and RS memory behavior that possibly realized the automatic conversion from short-term memory to long-term memory in bio-inspired computing does not fully explore. The thorough analysis of the coexistence of NDR effect and RS memory behavior by memristor model offers a chance for the efficient hardware implementation to faithfully mimic the function of biological brain, such as learning, memory, and cognition. A highly accurate compact dynamical model with the S-type NDR effect was developed in Ref. [23], which can serve as selectors in emerging non-volatile crossbar memory arrays. In Ref. [24], a parallel memristor model was proposed after fabricating the two-terminal metal-oxide-metal devices, enabling a systematic analysis of the coexistence of NDR effect and RS memory behavior. A practical model of NbO_2-based mott memristor with the typical NDR effect was designed, it was ideal for circuit-theoretic investigations [25]. However, these models are complex and do not consider an explicit relationship between current and voltage, which are unsuitable for application in bio-inspired computing systems. Reference [26] reported on a novel TiO_x-based memristive model considering the drifting effect, diffusion, and NDR behavior. This model attempted to balance complexity and accuracy, while seldom considered the physical mechanism of the coexistence of physical effect and RS memory behavior. Based on this, a physics-oriented memristor model with the coexistence of NDR effect and RS memory behavior for bio-inspired computing is proposed. The main contributions of this study are as follows:

1) The Ag/TiO_x/FTO memristor is prepared using sol-gel and magnetron sputtering method. It provides the physical support for the subsequent model construction. Meanwhile, a detailed electrochemical analysis is carried out, indicating that the coexistence of NDR effect and RS memory behavior memory behavior can be modulated by the moisture with a good reversibility at room temperature.
2) The physics-oriented mathematical model of the Ag/TiO_x/FTO memristor is constructed, which provides the possibility to explore the dynamics of the coexistence of NDR effect and RS memory behavior in simulation and help realize the deep integration of physical memristors into bio-inspired computing systems and energy-efficient integrated circuits.
3) Considering the coexistence of physical effect and RS memory behavior, the prepared memristor can be applied to associative memory, enabling a full-hardware implementation of affective computing to be feasible and simple.

2. Preparation and testing

2.1. Preparation of Ag/TiO_x/FTO memristor

The memristor is fabricated using the sol–gel method and the magnetron sputtering method. The former method is used to prepare the TiO_x functional layer, while the latter method is used to synthesize the Ag and FTO electrodes. The fabrication process (as shown in Fig. 1) can be summarized in the following steps:

Step 1 : The surface of the FTO substrate is cleaned with deionized water and ethyl alcohol thrice to remove any possible contaminants.
Step 2 : Plasma machine (PDC-32G-2) is adopted to the cleaned surface of the FTO substrate for 30 s.
Step 3 : 350 μL of $C_{12}H_{28}O_4Ti$, 5 mL of C_3H_8O, and 25 μL of HCl are mixed and continuously stirred using a magnetic stirrer for 12 h to fabricate the precursor.
Step 4 : The FTO glass substrate is placed on a spin coater in vacuum. The mixed precursor is continuously spin-coated on the patterned FTO glass substrate at 4,500r/min for 60 s.
Step 5 : The FTO substrate is transferred to a muffle furnace and annealed at 550 °C in ambient atmosphere for 3 h. This leads to the formation of a blue grey TiO_x film on the substrate.
Step 6 : Magnetron sputtering is used to fabricate the Ag electrode (diameter = 200 μm, thickness = 150 nm) on the TiO_x functional layer. In this manner, the Ag/TiO_x/FTO memristor is fabricated.

2.2. Performance test of Ag/TiO_x/FTO memristor

Based on the prepared Ag/TiO_x/FTO memristor, the necessary performance testing is further carried out. The electrical characteristics of Ag/TiO_x/FTO memristor is tested on an electrochemical workstation (CHI-660D) with a probe station (Lake Shore TTPX). The workstation is used to measure the current–voltage (I–V) characteristics of the device, and the probe station is used to test the relative humidity (RH) of air. We generate an experimental environment with three different RH levels: 1) RH of 0% (dry ambient) by injecting synthetic air (20% O_2, 80% N_2, and H_2O < 5 ppm) through three interconnected heated glass-delivery

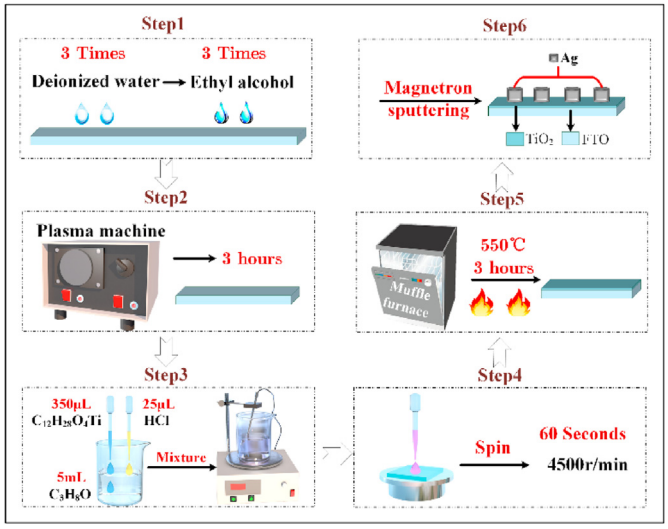

Fig. 1. Preparation process of the Ag/TiOx/FTO memristor.

tubes filled with dry CaO nano-powders; 2) RH of 35% (ambient RH of the laboratory); 3) RH of 95% (moist ambient) by passing laboratory air into a gas washing bottle containing deionized water.

The curve has a bias voltage of ±6 V and scan rate of 1 V/s in steps of 0.025 V. The bias voltage sweep sequence is 0 V → −6 V → 0 V → 6 V → 0 V. The memristor exhibits typical RS memory behavior under a RH of 0%, as shown in Fig. 2(a), and the inset is a structural representation of the Ag/TiO$_x$/FTO memristor. As the RH is increased to 35%, the device exhibits a significant NDR effect in the positive voltage region with a maximum current I_p of approximately 35 mA, a valley current I_v of approximately 25 mA, and a compliance current I_{cc} of approximately 50 mA (Fig. 2(b)). As observed in Fig. 2(c), when RH reaches 95%, the device exhibits a strong coexistence of NDR effect and RS memory behavior in the positive voltage region with maximum current I_p increased to 85 mA, valley current I_v increased to 78 mA, and compliance current I_{cc} increased to 100 mA. To investigate the stability of the coexistence of NDR effect and RS memory behavior, a 1 V reading voltage is applied in the Ag/TiO$_x$/FTO memristor at RH of 95% for 10^4 s, as shown in inset of Fig. 2(c). During the retention time, a resistance ratio between the high-resistance state (HRS) and low resistive state of HRS/LRS@ I_p, HRS/LRS@ I_v, and HRS/LRS@ I_{cc} is about 50, 20, and 100 respectively indicating that the coexistence of NDR effect and RS memory behavior has good stability.

To investigate the sensitivity of the Ag/TiO$_x$/FTO memristor to moisture, the I–V measurements were repeated with different RH levels (Fig. 3). The coexistence phenomena disappeared at a RH of 0% but reappeared and then gradually increased with RH, having the most significant effect at 95%. This indicates that the RS memory behavior and the NDR effect can be simultaneously triggered in the Ag/TiO$_x$/FTO memristor at room temperature, and the coexistence of NDR effect and RS memory behavior is affected by the RH.

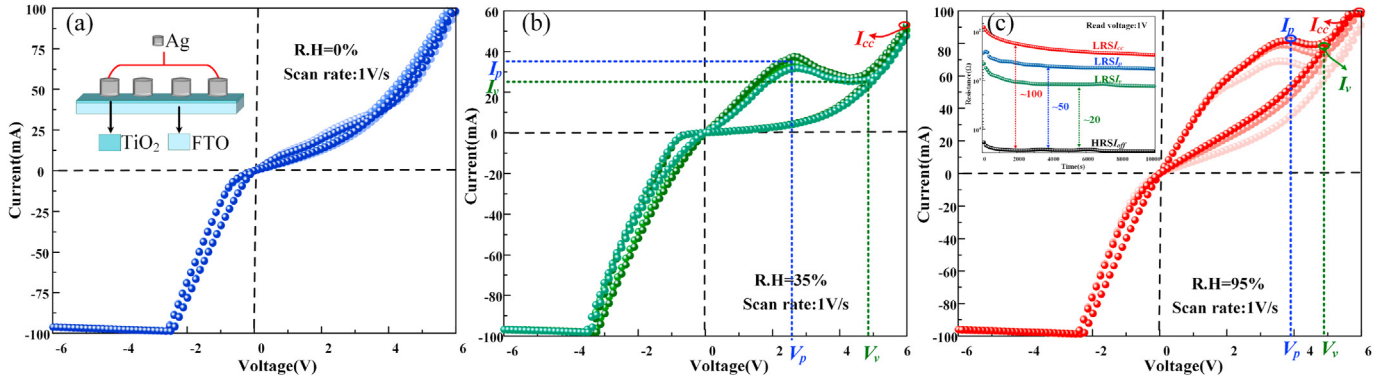

Fig. 2. The performance test of Ag/TiO$_x$/FTO memristors. (a) *I–V* curves of Ag/TiO*x*/FTO memristor under a RH of 0%; (d) *I–V* curves of Ag/TiO*x*/FTO memristor under a RH of 35%; (e) *I–V* curves of Ag/TiO*x*/FTO memristor under a RH of 95%.

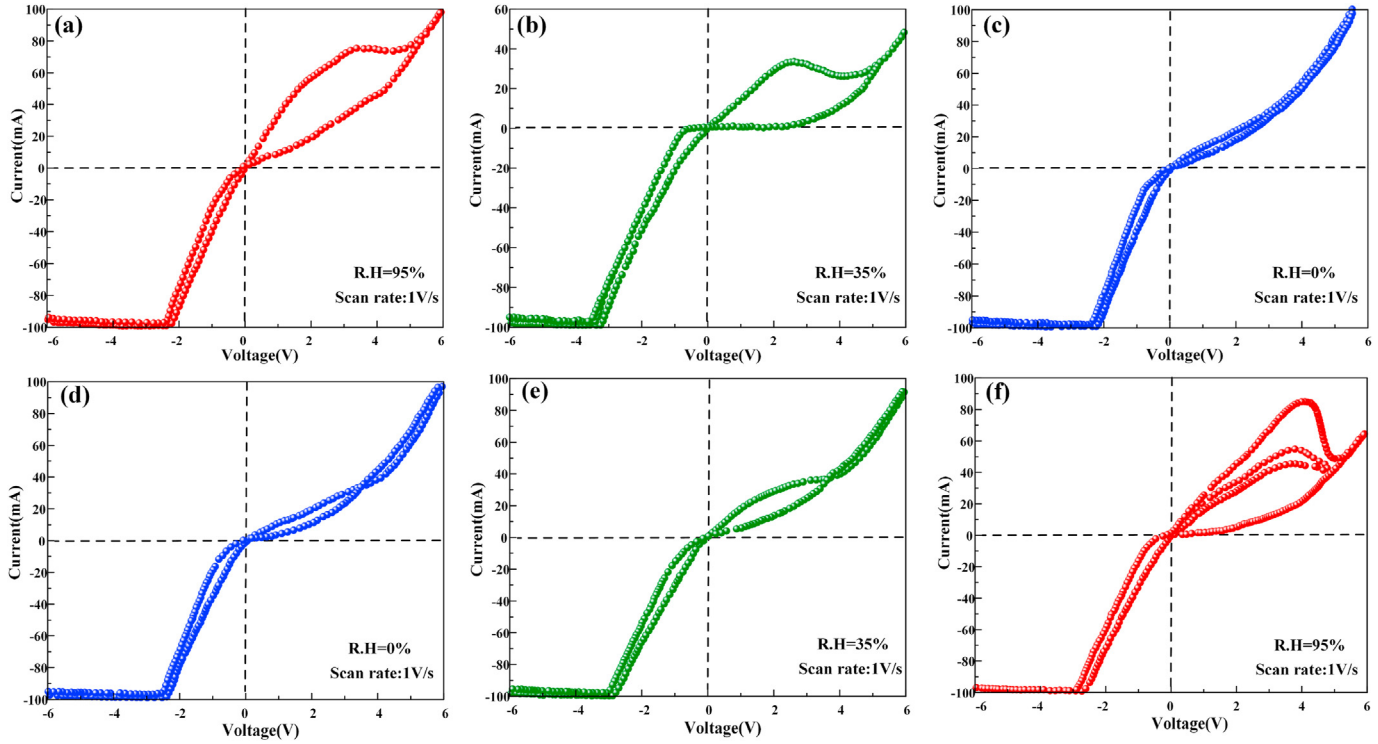

Fig. 3. *I–V* curves of Ag/TiO$_x$/FTO memristor under different RH levels: (a) RH = 95%; (b) RH = 35%; (c) RH = 0%; (d) RH = 0%; (e) RH = 35%; (f) RH = 95%.

3. Metristor modeling

3.1. Analysis of physical mechanism of memristor

To explain the influence of the Ag/TiO_x/FTO memristor to moisture, this paper further analyzed the physical mechanism involving the migration of Ag^+, oxygen vacancy (V_o), and water-related reaction process.

Fig. 4(a) illustrates the I–V curve of the Ag/TiO_x/FTO memristor plotted at RH of 95%. The trend can be divided into five sections: (i) scan voltage from 0 V to −6 V; (ii) scan voltage from −6 V to V_p (the voltage corresponding to the maximum current I_p of the NDR); (iii) scan voltage from V_p to V_v (the voltage corresponding to the valley current I_v of the NDR); (iv) scan voltage from V_v to +6 V; (v) scan voltage from +6 V to 0 V. In part (i), the memristor is in the HRS. V_o at the TiO_x/FTO interface gradually migrates towards the Ag electrode and forms the V_o conduction path. Meanwhile, the H_2O molecules at the Ag/TiO_x interface produce OH^- when V_o is applied. These ions move along the grain boundaries of TiO_x and migrate towards the FTO electrode. The dynamic migration of V_o and OH^- results in the memristor switching from the HRS to the LRS, signaling the completion of the "SET" process (Fig. 4(b)). In part (ii), the memristor remains in the LRS. When the voltage is varied from −6 V to 0 V, the conduction path established by V_o is enhanced. When the voltage is varied from 0 V to V_p, Vo gradually returns to the side of the FTO electrode, indicating the gradual breaking of the path. Meanwhile, the Ag^+ ions from the Ag electrode migrate towards the FTO electrode, where they are reduced to Ag. Thus, metallic conduction filaments are gradually produced with the steady agglomeration of Ag. Note that the Vo conduction path is established in the direction opposite to that of the Ag filament, representing a pair of competing modes. Before the path is broken, the device reaches the peak current I_p (Fig. 4(c)). In part (iii), the V_o conduction path is ruptured, and the device current is solely generated by Ag conduction filaments. The current decreases from the peak current I_p to the valley current I_v. (Fig. 4(d)). In part (iv), the increasing positive voltage leads to the production of more Ag filaments, which elevates the current to the compliance value I_{cc} (Fig. 4(e)). In part (v), when the voltage is varied from +6 V to 0 V, the metallic conduction path is disintegrated, and the memristor changes from the LRS to HRS, signaling the completion of the "RESET" process (Fig. 4(f)).

Based on this, the coexistence of NDR effect and RS memory behavior in Ag/TiO_x/FTO memristors is governed by the migration of V_o, as well as the formation and rupture of metallic (Ag) filaments from a micro perspective. OH^- ions are generated by H_2O molecules on interaction with the surface V_o. Then, the grain boundaries of TiO_x are broadened by the OH^- migration, accelerating the migration of Ag^+ and V_o.

When a negative voltage is applied to the Ag/TiO_x/FTO memristor, the RS phenomenon is governed by the conduction path formed by oxygen vacancy migration, satisfying the space-charge limited current (SCLC) mechanism [27] with the following mathematical expression:

$$J \propto \frac{V^{m+1}}{L^{2m+1}} \tag{1}$$

where J is the current density, V denotes the external voltage, L denotes the microwire's length, and m is a fitting parameter.

When $m = 0$, the current is linearly related to the voltage, demonstrating an Ohmic or Ohmic-like conduction law. When a positive voltage is applied to the Ag/TiO_x/FTO memristor, the RS memory behavior and NDR effect coexist due to the effects of both oxygen vacancy migration and Ag conduction filament formation, satisfying the SCLC and Schottky tunnelling mechanisms [28]. The Schottky tunnelling model is described by the following equations:

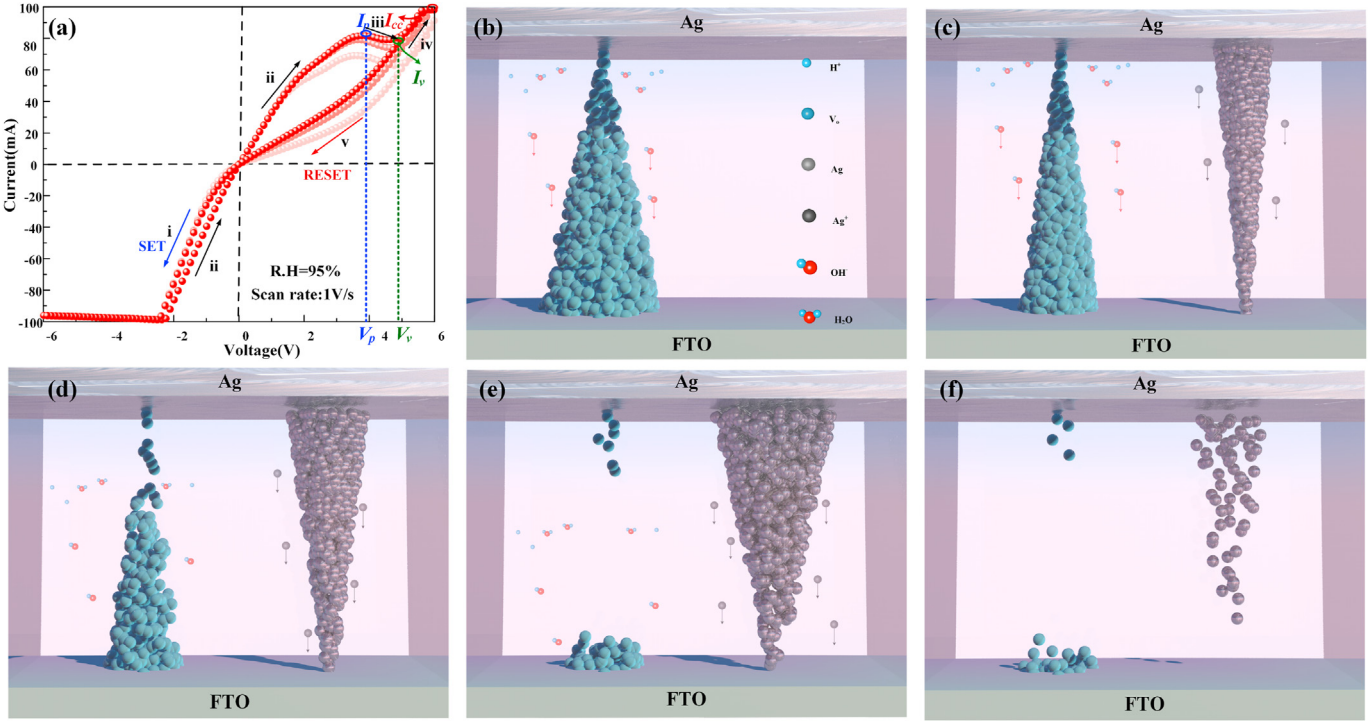

Fig. 4. Schematic diagram of physical mechanism for the coexistence NDR effect and RS memory behavior observed in Ag/TiO_x/FTO device: (a) Typical *I–V* curve can be divided into five sections; (b) The physical mechanism of part (i); (c)The physical mechanism of part (ii); (d) The physical mechanism of part (iii); (e) The physical mechanism of part (iv); (f)The physical mechanism of part (v).

$$J \propto \exp\left(\frac{\beta}{K_B T} E^{\frac{1}{2}} - \frac{\varphi}{K_B T}\right) \tag{2}$$

$$\beta = \sqrt{\frac{q^3}{4\pi\varepsilon_0\varepsilon_r}} \tag{3}$$

where φ denotes the Schottky barrier, K_B denotes the Boltzmann constant, T denotes the temperature, E denotes the electric field, q denotes the electric charge, and ε_0 and ε_r represent the vacuum permittivity and relative permittivity, respectively.

3.2. Demonstration of PSpice analysis

Based on this analysis, a physics-oriented model of Ag/TiO_x/FTO memristor is constructed for the element to explore the dynamics of the coexistence of NDR effect and RS memory behavior in simulation. The relationship between current and voltage can be concluded as follows:

$$i_{Gm}(t) = \begin{cases} a_1 x(t)^{n_1} v(t) + a_2\left(1 - x(t)^{n_2}\right)\left(1 - e^{-m_1 v(t)}\right), v(t) \geq 0 \\ a_3 x(t)^{n_3} v(t) + a_4\left(1 - x(t)^{n_4}\right) v(t)^{m_2}, v(t) < 0 \end{cases} \tag{4}$$

where $v(t)$ denotes the applied voltage, $i_{Gm}(t)$ denotes the current in the memristive device, and a_1, a_2, a_3, a_4, n_1, n_2, n_3, n_4, m_1, and m_2 are the fitting parameters of the model used such that the I–V response curve of the mathematical model could approximate the actual physical model. The right-hand side of (4) represents the parallel conductive channels. Specifically, for the positive voltage region, the right-hand side of (4) represents the Ohmic and Schottky tunnelling currents. For the negative voltage region, the right-hand side of (4) represents the Ohmic and SCLC currents, respectively. $x(t)$ denotes the state variable for characterizing the conductivity of the device, where $x \in [0,1]$. The value of $x(t)$ is derived by integrating the current $i_{Gx}(t)$ over time through capacitor C_x in the equivalent circuit.

Reference [29] demonstrated that the ion migration behavior in a memristor under an applied electric field satisfies the following exponential relationship:

$$\frac{dx}{dt} \propto \sinh\left(\frac{v/E_0}{D - x}\right) \tag{5}$$

where v denotes the applied voltage, x denotes the state variable, D denotes the layer thickness of the memristor, and fitting parameter E_0 represents the characteristics of the electric field.

Inspired by (5), a change in the state variable can be mathematically expressed as:

$$i_{Gx}(t) = \frac{dx}{dt} = \begin{cases} \alpha \sinh \beta v(t) f_{off}(x) - \gamma x, v(t) > 0 \\ \alpha \sinh \beta v(t) f_{on}(x) - \gamma x, v(t) \leq 0 \end{cases} \tag{6}$$

where α is the fitting parameter, and the larger its magnitude, the faster the rate of change of the state variable. β denotes the voltage control parameter, and γ denotes the effect of different levels of RH on the ionic migration and Vo diffusion. $f_{off}(x)$ and $f_{on}(x)$ representing the window functions [18] mainly used to ensure that the state variable $x(t)$ is always in the range of [0,1] and are expressed as follows:

$$\begin{cases} f_{\text{off}}(x) = \exp\left[- \exp\left(\frac{x - a_{\text{off}}}{w_c}\right)\right], v(t) > 0 \\ f_{\text{on}}(x) = \exp\left[- \exp\left(\frac{a_{\text{on}} - x}{w_c}\right)\right], v(t) \leq 0 \end{cases} \tag{7}$$

where w_c, a_{off}, and a_{on} are all fitting parameters.

3.3. Simulation analysis of memristor model

To measure the fit between the experimental data of the Ag/TiO_x/FTO memristor and the proposed circuit model, we used gradient descent and minimized the relative error function value [30]. The error function is selected as the relative root mean squared error (RRMSE):

$$E_{rrms} = \sqrt{\frac{1}{N}\left(\frac{\sum_{k=1}^{N}\left(V_k - V_{ref,k}\right)^2}{V_{ref}^2} + \frac{\sum_{k=1}^{N}\left(I_k - I_{ref,k}\right)^2}{I_{ref}^2}\right)} \tag{8}$$

where N denotes the total number of samples, V_k and $V_{ref,k}$ denote the k_{th} voltage applied to the terminals of the memristor and the circuit model, respectively. I_k and $I_{ref,k}$ represent the k_{th} current through the memristor and circuit model, respectively. V_{ref} and I_{ref} are the Euclidean norms of voltage and current of the circuit model, respectively.

The fitting results of the memristor are depicted in Fig. 5, where the solid spheres represent the experimental data obtained from the Ag/TiO_x/FTO memristor, and the solid lines represent the I–V curves of the constructed circuit model. Here, the following parameters of the circuit model are obtained using sequential model-based global optimization (SMBO) [31]: $a_1 = 4.614 \times 10^{-3}$, $a_2 = -0.105$, $a_3 = 0.040$, $a_4 = 7.035 \times 10^{-5}$, $n_1 = 3.300 \times 10^{-12}$, $n_2 = 0.160$, $n_3 = 0.051$, $n_4 = 90.074$, $m_1 = -0.460$, $m_2 = 4.818 \times 10^{-3}$, $\alpha = 1.763$, $\beta = 0.729$, $a_{on} = 0.255$, $a_{off} = 0.576$, and $w_c = 0.141$. The initial value of state variable $x(t)$ is 0. Fig. 5(a) illustrates the simulation results of the device under a RH of 0%. In this environment, the model parameter γ is 0.012, and the device exhibited a typical RS phenomenon. The RRMSE obtained after fitting the theoretical results to the experimental data is 0.14%. When the RH is increased to 35%, the model parameter γ is 0.037, and the symmetrical, weaker coexistence of NDR effect and RS memory behavior is observed in the positive voltage region (Fig. 5(b)). In this region, the fitted curve matched the target data closely and the RRMSE obtained is 0.46%. When the RH is increased to 95%, the model parameter γ is 0.088, and the combined effects of NDR effect and RS memory behavior observed in the positive voltage region are relatively stable and significant (Fig. 5(c)). Compared with Fig. 5(b), the peak current I_p of the memristor in Fig. 5(c) increased from 25 to 85 mA, and the RRMSE is 0.48%.

In Fig. 5(d), when a triangular-wave voltage is applied to the memristor, the overall current through the device tended to increase in the positive voltage region but decreased in the negative voltage region. The same trend of current variation can be observed in Fig. 5(h) and (k). The coexistence of NDR effect and RS memory behavior disappeared under a RH of 0% (Fig. 5(e)). When the RH is increased to 35%, a feeble synergy between NDR effect and RS memory behavior is observed in the positive voltage region with a more pronounced migration (Fig. 5(i)). When the RH is increased to 95%, the NDR effect and RS memory behavior shared a strong synergy (Fig. 5(l)). This is because the OH^- migration broadened the electrical channel, enhancing the migration of Ag^+ and V_o along the boundary. The internal state variable $x(t)$ tended to change

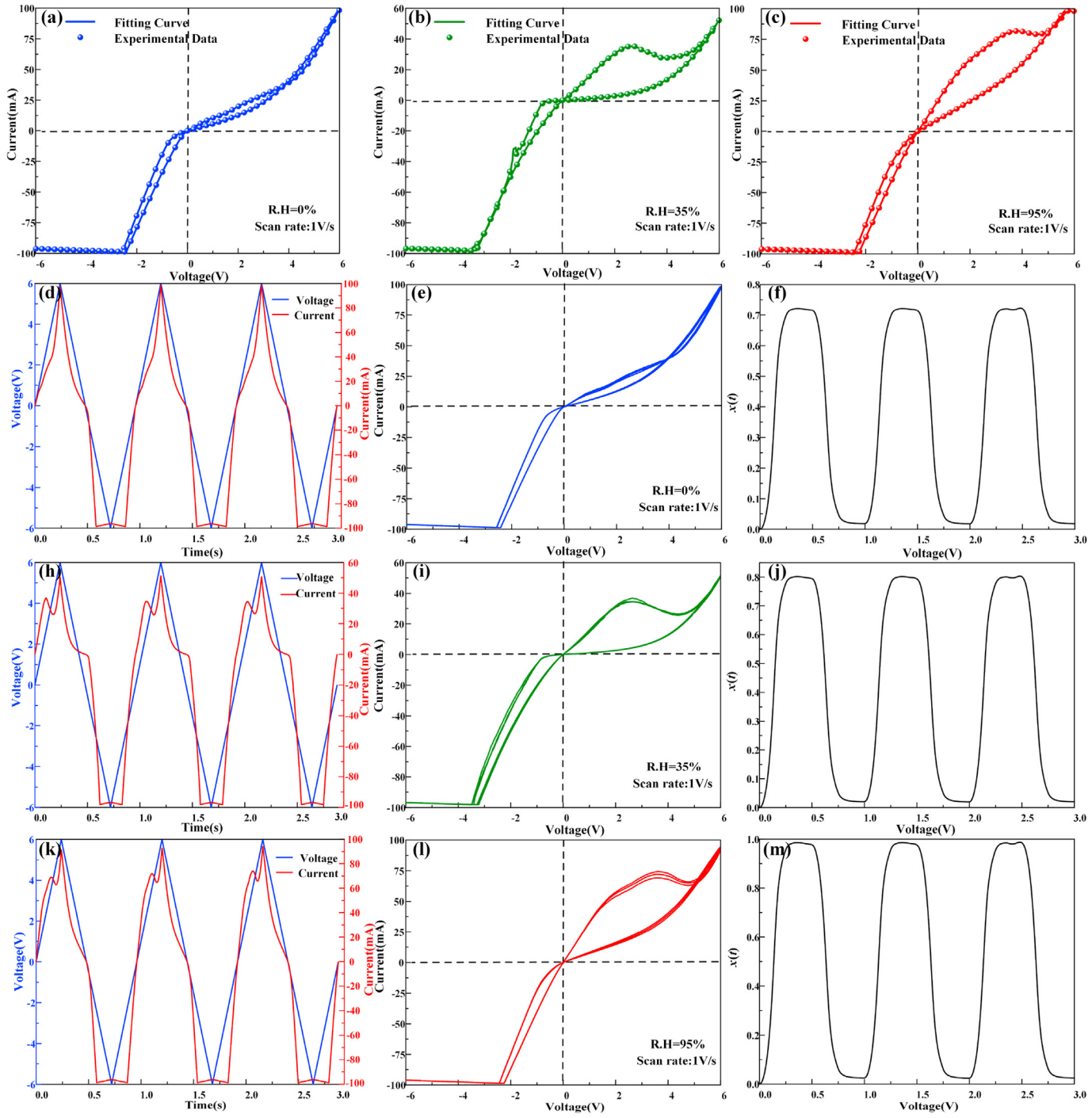

Fig. 5. Simulation results of the physical-oriented memristor model (a) The fitting result of Ag/TiOx/FTO memristor under a RH of 0%; (b) The fitting result of Ag/TiOx/FTO memristor under a RH of 35%; (c) The fitting result of Ag/TiOx/FTO memristor under a RH of 95%; *t*-*V*&*I* under RH of 0%; (b) *V*–*I* under RH of 0%; (c) *t*-*x* under RH of 0%; (d) *t*-*V*&*I* under RH of 35%; (e) *V*–*I* under RH of 35%; (f) *t*-*x* under RH of 35%; (g) *t*-*V*&*I* under RH of 95%; (h) *V*–*I* under RH of 95%; (i) *t*-*x* under RH of 95%.

identically for all the three RH levels, as shown in Fig. 5(f), (j) and (m). When the input voltage is positive, $x(t)$ tended to increase, and vice versa. In particular, enabled $x(t)$ to reach its upper and lower boundaries during the change under a RH of 95%.

A comparative summary of different memristive models is given in Table 1.

Different memristor models based on quantum tunnelling theory were proposed to analysis the coexistence of NDR effect and RS memory behavior [23–25]. However, these models are complex, without an explicit relationship between current and voltage, and are not suitable for further application in bio-inspired computing. Another simplified model has recently been proposed, considering the drifting effect, diffusion, and NDR behavior [26]. In this model, the coexistence of NDR and RS cannot be regulated by changing a single parameter. The current mainstream memristor models (i.e., linear memristor model [18] and voltage threshold adaptive memristor (VTEAM) model [22]) have become renowned for their simplicity, generality, accuracy, and low computational complexity.

Table 1
Comparative summary of different memristive models.

Reference	[18]	[19]	[20]	[21]	[25]	[28]	This work
State variable	No physical explanation	Core temperature	Ambient temperature	$a_{off} \le x \le a_{on}$ Undoped region width	$a_{off} \le x \le a_{on}$ Undoped region width	$0 \le x \le 1$ No physical explanation	$0 \le x \le 1$ Conductivity of the device
Control mechanism	Electric field	Charge	Voltage	Voltage	Voltage	Voltage	Voltage
I–V relationship	Ambiguous	Ambiguous	Ambiguous	Explicit	Explicit	Explicit	Explicit
Physical mechanism	QTT	QTT	QTT	Ambiguous	IMT	Ambiguous	QTT&SCLC
Model Complexity	Complex	Complex	Complex	Medium	Easy	Medium	Medium
Boundary effects	No	No	No	Unsolved	Solved	Solved	Solved
Threshold effects	No	NO	No	No	No	Yes	Yes
NDR effects	Yes	Yes	Yes	Yes	No	No	Yes
Fitting accuracy	High	High	High	Moderate	Low	Moderate	High
Applied rang	Narrow	Narrow	Narrow	Wide	Wide	Wide	Wide

Note: IMT→Ion migration theory; QTT→Quantum tunnelling theory; SCLC→Space-charge limited current.

However, these models [18,22] seldom consider the physical mechanism of the real memristor and the physical phenomena including the coexistence of NDR effect and RS memory behavior. Compared with other works, the proposed model is a simple, flexible and convenient model that can fit practical memristive devices better than previously proposed models and improve the simulation runtime, with a RRMSE of 0.48%. These results are dependent on the particular fitting parameters. A lower value for a_{on} and a_{off} produces lower accuracy and enhanced computational runtime [22]. The proposed model exhibits a voltage threshold and nonlinear dependences on the state variable which alleviates the boundary effects and shows the coexistence of NDR and RS memory behavior. This model fits practical memristive devices better than previously proposed models. The proposed model is suitable for bio-inspired computing.

4. A memristor-based affective computing circuit

Emotion is central to the quality and range of everyday human experience [32]. According to the theories of psychology [33,34], the human brain can establish the connections between emotion and external stimulus (such as text, sound and image). Notably, the fabricated memristor exhibits obvious the coexistence of NDR effect and RS memory behavior under a RH of 95% which provides multiple stable resistance states and can adjust memory time without additional circuit and cost, enabling a fully hardware-implemented memristor-based affective computing circuit to be feasible and simple.

4.1. Circuit design

This paper presents a thought experiment on the emotional response of human beings, which intend to use as the application basis for designing the affective computing circuit with the prepared memristor. A person may not express a specific emotional response to message notifications. However, depending on the nature of the message ("good" or "bad"), they may feel happy or sad. Suppose that a person receives only "good" messages for a certain period. On receiving a message notification thereafter, s/he will assume the message to be "good" without reading its contents and will feel happy. Conversely, if a person receives only bad messages for a certain period, s/he will respond with angst on receiving a notification after that period. If there are no message notifications for a long period, the established associations of a person's "happiness" and "sadness" will cease. Furthermore, the person's emotional response will not fluctuate when s/he receives a new message notification. To more intuitively represent this emotional change process, Fig. 6(a) summarizes the relevant information.

Based on the information in Fig. 6(a), this paper further constructs an affective computing circuit based on the prepared Ag/TiO_x/FTO memristor to simulate the process of emotional response change in this hypothetical scenario (as shown in Fig. 6(b)).

In Fig. 6(b), the proposed circuit consists of four parts, namely the input module, logic module, calculation module, and output module. The logic module includes two XOR gates, which are mainly used to change the state of the input signals. The calculation module contains two memristors, M_1 and M_2 (with high-resistance state HRS and three low resistive states LRS@ I_p, LRS@ I_v, and LRS@ I_{cc}), two conventional resistors, R_1 and R_2, and two transistors (with control voltage g). The circuit has three inputs and two outputs, where the inputs US_1, MS, and US_2 represent the "good" message, message notification, and "bad" message signals, respectively. Each input has two states, i.e., high-voltage state V_H and low-voltage state V_L. Specifically, the inputs US_1, MS, and US_2 are in V_H, indicating that the person receives the corresponding signals; conversely, the three inputs are all in V_L, indicating that they receive no signal. The outputs are represented by the output voltages V_{out1} and V_{out2}. When V_{out1} (V_{out2}) is in V_H, the person is "happy" ("sad"). When the voltages are in V_L, the person does not exhibit any change in their emotional response. To stimulate the process of change in human emotional responses, this paper assumes that LRS@ $I_{cc} = R_1 = R_2 \ll$ HRS, and the initial resistance of both M_1 and M_2 is HRS.

4.2. Results and discussion

Fig. 6(c) depicts the results according to the experiment setup. For clarity, the simulation results are classified into six stages (Initial state, Test 1, Learning, Test 2, Forgetting, and Test 3).

In Initial state (0s–8s), when the control signal g is in V_H, the branch circuit of M_1 is connected, the input signal US_1 (red solid line) remains in V_H while MS (yellow solid line) remains in V_L. The output signal V_{out1} (pink solid line) is also in V_H, implying that the person feels happy after s/he receives a "good" message. However, when g is in V_L and the branch circuit of M_2 is connected, US_2 (blue solid line) remains in V_H while MS (yellow solid line) is the opposite. The output signal V_{out2} (green solid line) is in V_H as well, indicating that the person feels sad after s/he received a "bad" message.

During Test 1 (8s–15s), when US_1 and US_2 are in V_L but MS is in V_H, both V_{out1} and V_{out2} enter the low state V_L. We conclude that the person's emotion does not significantly fluctuate when s/he receives the message notification. Note that M_1 (purple solid line) and M_2 (green solid line) are always in HRS during the above two processes.

At the Learning stage (15s–23s), when signal g is in the high state V_H and the branch circuit of M_1 is connected, MS is injected

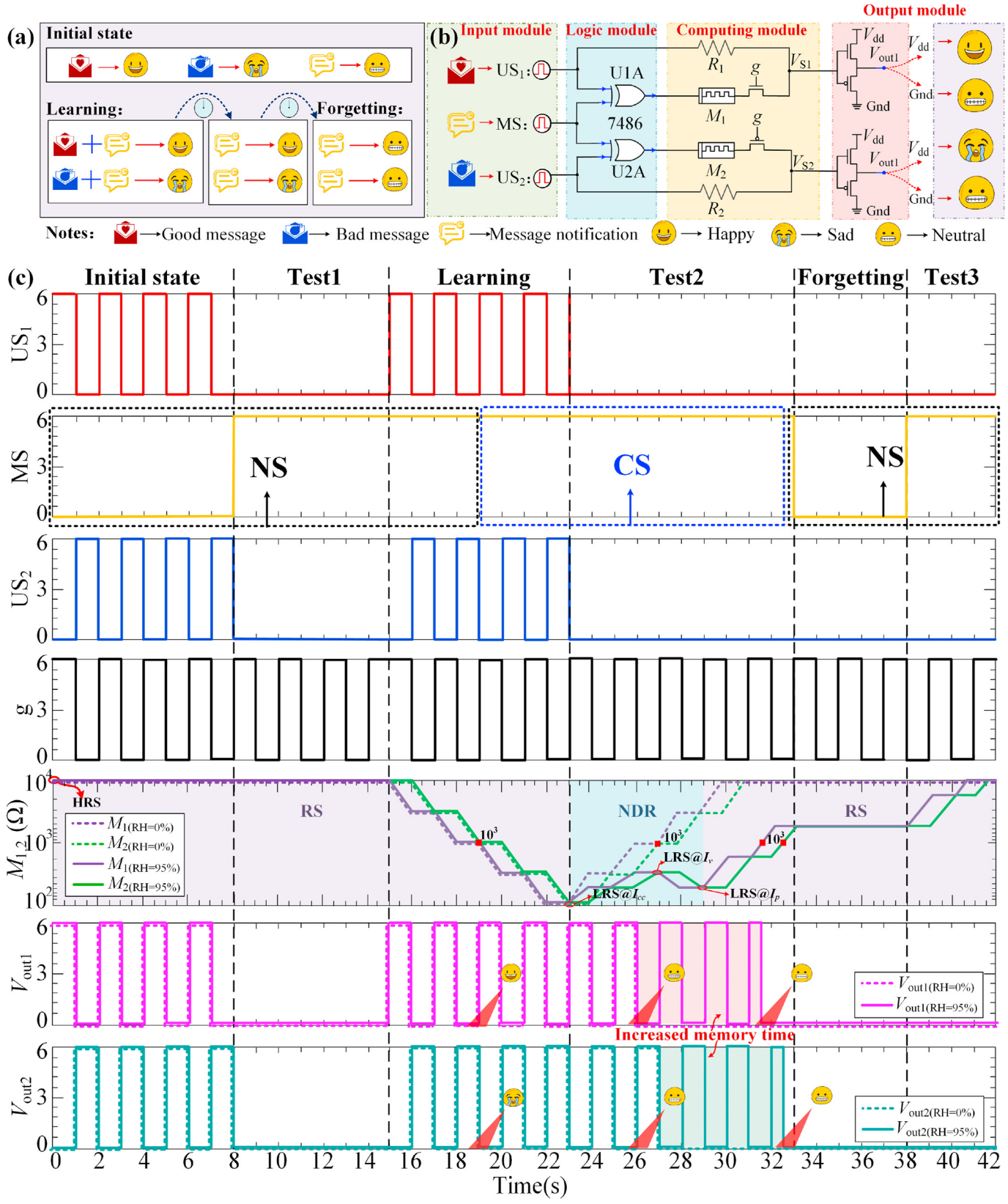

Fig. 6. A fully hardware-implemented affective computing circuit for bio-inspired computing (a) The collected information of affective associative learning experiment; (b) Affective computing circuit based on Ag/TiO_x/FTO memristor; (c) Simulation result of affective computing circuit based on Ag/TiO_x/FTO memristor.

Table 2
Comparison of different memristor-based bio-inspired computing circuits.

Reference	Metristor model	Switching type	Complexity	Automatic conversion	Applications
[12]	Pt/Ag/SiOx:Ag/Ag/Pt	RS	Simple	No	Hebbian-like learning
[13]	Ag/TCNC/FTO	RS	Simple	No	Nonvolatile memory
[14]	NbO_x-based memristor	NDR + RS	Simple	No	Boolean operations
[15,16]	TiO_x-based memristor	NPC + RS	Simple	No	Vision sensor
[35]	VTEAM model	RS	Complex	No	Associative learning
[39]	Ag/HfO_x/ITO	TS/RS	Simple	No	Associative learning
[36,37]	VTEAM model	RS	Complex	No	Affective computing
[38]	Linear memristor model	RS	Complex	No	Affective computing
This work	Ag/TiO_x/FTO	NDR + RS	Simple	STM to LTM	Affective computing

into the circuit before US_1, and M_1 tend to LRS@ I_{cc}. V_{out1} is a high-state signal synchronized with US_1, implying the happy state of the person. Especially when t ≈ 19s, only MS is assigned to the person, and V_{out1} is in the high state V_H. At this time, M_1 approximately equals to $10^3\Omega$ (i.e., the threshold resistance). This suggests that the person has established the corresponding associative memory at that moment, and the message notification changed from neutral stimulus (NS) to conditional stimulus (CS). Similarly, when g is in the opposite state, the circuit retrieved the corresponding associative memory after learning the "bad" message and message notification.

As for Test 2 (23s−33s), when the control signal g is in V_H, the branch circuit of M_1 is connected and MS remains in the high state V_H while US_1 remains in the low state. M_1 gradually increases from LRS@ I_{cc} to LRS@ I_v, then decreases to LRS@ I_p within a short time, after that M_1 will exceed the threshold resistance $10^3\Omega$. During this time, V_{out1} is synchronized with the control voltage g, indicating that the person feels happy by simply receiving the message notification. Once M_1 tends to the threshold resistance, V_{out1} quickly goes down to the low state V_L, indicating that the established associative learnings fades, person does not exhibit any change in their emotional response after s/he received another message notification. Similarly, the associative memory of the person forms by the message notification and sadness changed from present to absent.

During Forgetting stage (33s−38s), when the input signals US_1, US_2, and MS, as well as the output signals V_{out1} and V_{out2} are all in the low state V_L, M_1 and M_2 are maintained at 1.2 kΩ. The results demonstrate a lack of change in the emotional response of the person when they do not receive a message.

During Test 3 (38s−42s), when g is in the high state and M_1 increases from 1.2 kΩ to HRS, V_{out1} remains in the low state V_L. As a result, when the person receives only the message notification, her/his emotions do not fluctuate and the message notification becomes an NS. When g is low and M_2 changed from 1.2 kΩ to HRS, V_{out2} remains in the low state V_L and the same outcomes are obtained.

To further explore the influence of the coexistence of NDR effect and RS memory behavior, a comparative experiment under a RH of 0% is conducted, the corresponding results (represented by dash line) as shown in Fig. 5(c). It is worth noting that the results of M_1, M_2, V_{out1} and V_{out2} from the Initial stage, Test1, and Learning stage are the same as the results under a RH of 95%. Due to the memristors only exhibit typical RS memory behavior under a RH of 0%, M_1 and M_2 are continuously increased from LRS@ I_{cc} to the HRS without downward changes in Test 2. During this process, V_{out1} is synchronized with the control voltage g and V_{out2} is contrary with the control voltage g, until M_1 and M_2 tend to the threshold resistance, V_{out1} and V_{out2} quickly go down to the low state V_L. During the Forgetting stage and Test3, M_1 and M_2 are maintained in HRS and V_{out1} and V_{out2} remain in the low state V_L. The comparative experiment demonstrates that the coexistence of NDR effect and RS memory behavior memory behavior can increase memory time without additional circuit and cost. Furthermore, proper humidity adjustment can change the memory time, which is expected to realize the automatic conversion from short-term memory to long-term memory in bio-inspired computing.

A comparison between different memristor-based bio-inspired computing circuits is provided in Table 2. It is clear that all these above-mentioned implementations have proved effective in high-level simulation of the biomimetic or neuromorphic computing. References [35,36−38] directly use the mathematical memristor model (i.e., the VTEAM model and linear memristor model) to mimic the brain function, such as forgetting, learning, and memory. But the specific circuit design is complex and does not consider the physical characteristics of memristor, leading to high energy consumption and large computational overhead. Meanwhile, references [14−16] and our work all discuss the coexistence of physical effect (i.e., the NDR and NPC effect) and RS memory behavior, while only our work further utilizes this coexistence phenomenon to realize the automatic conversion from STM to LTM in bio-inspired computing, which may be helpful in reducing additional circuit components and energy consumption.

Based on these, the proposed fully hardware-implemented memristor-based affective computing circuit is a simple, flexible, and convenient one that can adjust memory time without additional circuit and cost, enabling the automatic conversion from STM to LTM in bio-inspired computing to be feasible.

5. Conclusion

This work presents an investigation of a physics-oriented memristor model with coexistence of NDR effect and RS memory behavior for bio-inspired computing. Firstly, the Ag/TiO_x/FTO memristor is prepared using sol-gel method and magnetron sputtering method and its performance test indicates that the coexistence of NDR effect and RS memory behavior can be modulated by the moisture with a good reversibility at room temperature. Then, the corresponding dynamics in simulation are also explored by constructing a physical-oriented model of the Ag/TiO_x/FTO memristor. The accuracy of the proposed model is calibrated against the experimental data by tuning the fitting parameters, yielding an RRMSE of less than 0.48%. Furthermore, a memristor-based affective computing circuit is proposed, which contains emotional learning and forgetting features based on the corresponding biological mechanism of the human brain. The fabricated memristor exhibiting the coexistence of NDR effect and RS memory behavior provides multiple stable resistance states and can adjust memory time without additional circuit and cost. The future direction of research includes the development of bio-inspired computing

systems based on memristor and investigation of new techniques for the deep integration of nanomaterials science and the modern circuit theory.

Declaration of competing interest

The authors declare that they have no known competing financial interests or personal relationships that could have appeared to influence the work reported in this paper.

Acknowledgments

This work was supported in part by the National Natural Science Foundation of China under Grant 62001149 and Natural Science Foundation of Zhejiang Province under Grant LQ21F010009.

References

[1] R.B. Rashid, X. Ji, J. Rivnay, Organic electrochemical transistors in bioelectronic circuits, Biosens. Bioelectron. 190 (2021), 113461, https://doi.org/10.1016/J.BIOS.2021.113461.
[2] Y. Zhang, P. Qu, Y. Ji, W. Zhang, G. Gao, G. Wang, S. Song, G. Li, W. Chen, W. Zheng, F. Chen, J. Pei, R. Zhao, M. Zhao, L. Shi, A system hierarchy for brain-inspired computing, Nature 586 (2020) 378–384, https://doi.org/10.1038/S41586-020-2782-Y.
[3] A. Mehonic, A.J. Kenyon, Brain-inspired computing needs a master plan, Nature 604 (2022) 255–260, https://doi.org/10.1038/S41586-021-04362-W.
[4] T. Venkatesan, S. Williams, Brain inspired electronics, Appl. Phys. Rev. 9 (2022), 010401, https://doi.org/10.1063/5.0078798.
[5] X. Ji, Z. Dong, C.S. Lai, D. Qi, A brain-inspired in-memory computing system for neuronal communication via memristive circuits, IEEE Commun. Mag. 60 (2022) 100–106, https://doi.org/10.1109/MCOM.001.21664.
[6] Y. Wu, R. Zhao, J. Zhu, F. Chen, M. Xu, G. Li, S. Song, L. Deng, G. Wang, H. Zheng, S. Ma, J. Pei, Y. Zhang, M. Zhao, L. Shi, Brain-inspired global-local learning incorporated with neuromorphic computing, Nat. Commun. 13 (2022) 65, https://doi.org/10.1038/S41467-021-27653-2.
[7] G. Milano, G. Pedretti, K. Montano, S. Ricci, S. Hashemkhani, L. Boarino, D. Ielmini, C. Ricciardi, In materia reservoir computing with a fully memristive architecture based on self-organizing nanowire networks, Nat. Mater. 21 (2022) 195–202, https://doi.org/10.1038/S41563-021-01099-9.
[8] Z. Luo, Z. Wang, Z. Guan, C. Ma, L. Zhao, C. Liu, H. Sun, H. Wang, Y. Lin, X. Jin, Y. Yin, X. Li, High-precision and linear weight updates by subnanosecond pulses in ferroelectric tunnel junction for neuro-inspired computing, Nat. Commun. 13 (2022) 699, https://doi.org/10.1038/S41467-022-28303-X.
[9] C.D. Schuman, S.R. Kulkarni, M. Parsa, J.P. Mitchell, P. Date, B. Kay, Opportunities for neuromorphic computing algorithms and applications, Nat. Comput. Sci. 2 (2022) 10–19, https://doi.org/10.1038/S43588-021-00184-Y.
[10] S. Smys, J.M.R.S. Tavares, V.E. Balas, A.M. Iliyasu, Computational vision and bio-inspired computing, in: S. Smys, J.M.R.S. Tavares, V.E. Balas (Eds.), International Conference on Computational Vision and Bio Inspired Computing, Advances in Intelligent Systems and Computing, Springer Singapore, Singapore, 2019, pp. 304–311, https://doi.org/10.1007/978-981-16-9573-5.
[11] R. Yang, H.M. Huang, X. Guo, Memristive synapses and neurons for bio-inspired computing, Adv. Electron. Mater. 5 (2019), 1900287, https://doi.org/10.1002/AELM.201900287.
[12] Z. Wang, M. Rao, J.W. Han, J. Zhang, P. Lin, Y. Li, C. Li, W. Song, S. Asapu, R. Midya, Y. Zhuo, H. Jiang, J.H. Yoon, N.K. Upadhyay, S. Joshi, M. Hu, J.P. Strachan, M. Barnell, Q. Wu, H. Wu, Q. Qiu, R.S. Williams, Q. Xia, J.J. Yang, Capacitive neural network with neuro-transistors, Nat. Commun. 9 (2018) 3208, https://doi.org/10.1038/S41467-018-05677-5.
[13] T. Hussain, H. Abbas, C. Youn, H. Lee, T. Boynazarov, B. Ku, Y.R. Jeon, H. Han, J.H. Lee, C. Choi, T. Choi, Cellulose nanocrystal based bio-memristor as a green artificial synaptic device for neuromorphic computing applications, Adv. Mater. Technol. 7 (2022), 2100744, https://doi.org/10.1002/ADMT.202100744.
[14] S. Kumar, R.S. Williams, Z. Wang, Third-order nanocircuit elements for neuromorphic engineering, Nature 585 (2020) 518–523, https://doi.org/10.1038/S41586-020-2735-5.
[15] G. Zhou, B. Sun, X. Hu, L. Sun, Z. Zou, B. Xiao, W. Qiu, B. Wu, J. Li, J. Han, L. Liao, C. Xu, G. Xiao, L. Xiao, J. Cheng, S. Zheng, L. Wang, Q. Song, S. Duan, Negative photoconductance effect: an extension function of the TiOx-based memristor, Adv. Sci. 8 (2021), 2003765, https://doi.org/10.1002/ADVS.202003765.
[16] J. Li, Y. Zhang, C. Yao, N. Qin, R. Chen, D. Bao, Optoelectronic modulation of interfacial defects in lead-free perovskite films for resistive switching, Adv. Electron. Mater. 8 (2022), 202101094, https://doi.org/10.1002/AELM.202101094.
[17] T.D. Brown, S. Kumar, R.S. Williams, Physics-based compact modeling of electro-thermal memristors: negative differential resistance, local activity, and non-local dynamical bifurcations, Appl. Phys. Rev. 9 (2022), 011308, https://doi.org/10.1063/5.0070558.
[18] Z. Biolek, Z. Biolek, D. Biolek, V. Biolková, Spice model of memristor with nonlinear dopant drift, Radioengineering 18 (2017) 210–214.
[19] C. Yakopcic, T.M. Taha, G. Subramanyam, R.E. Pino, Generalized memristive device SPICE model and its application in circuit design, IEEE Trans. Comput. Aid D. 32 (2013) 1201–1214, https://doi.org/10.1109/TCAD.2013.2252057.
[20] O. Krestinskaya, A.P. James, L.O. Chua, Neuromemristive circuits for edge computing: a review, IEEE Transact. Neural Networks Learn. Syst. 31 (2020) 4–23, https://doi.org/10.1109/TNNLS.2019.2899262.
[21] KvatinskyS, E.G. Friedman, A. Kolodny, U.C. Weiser, TEAM: ThrEshold adaptive memristor model, IEEE Trans. Circuits Syst. I: Regular Papers 60 (2013) 211–221, https://doi.org/10.1109/TCSI.2012.2215714.
[22] KvatinskyS, M. Ramadan, E.G. Friedman, A. Kolodny, VTEAM: a general model for voltage-controlled memristors, IEEE Trans. Circuits Syst. II Express Briefs. 62 (2015) 786–790, https://doi.org/10.1109/TCSII.2015.2433536.
[23] G.A. Gibson, S. Musunuru, J. Zhang, K. Vandenberghe, J. Lee, C.C. Hsieh, W. Jackson, Y. Jeon, D. Henze, Z. Li, R. Stanley Williams, An accurate locally active memristor model for S-type negative differential resistance in NbOx, Appl. Phys. Lett. 108 (2016), 023505, https://doi.org/10.1063/1.4939913.
[24] X. Liu, P. Zhang, S.K. Nath, S. Li, S.K. Nandi, R.G. Elliman, Understanding composite negative differential resistance in niobium oxide memristors, J. Phys. D Appl. Phys. 55 (2022), 105106, https://doi.org/10.1088/1361-6463/AC3BF4.
[25] I. Messaris, R. Tetzlaff, A. Ascoli, R.S. Williams, S. Kumar, L. Chua, A simplified model for a NbO_2 Mott memristor physical realization, in: 2020 IEEE International Symposium on Circuits and Systems (ISCAS), Institute of Electrical and Electronics Engineers Inc., Seville, 2020, pp. 1–5, https://doi.org/10.1109/iscas45731.2020.9181036.
[26] J. Zhang, Z. Tang, N. Xu, Y. Wang, H. Sun, Z. Wang, L. Fang, A generalized model of TiOx-based memristive devices and its application for image processing, Chin. Phys. B 26 (2017), 090502, https://doi.org/10.1088/1674-1056/26/9/090502.
[27] F.D. Akgül, S. Eymur, Ü. Akın, Ö.F. Yüksel, H. Karadeniz, N. Tuğluoğlu, Investigation of Schottky emission and space charge limited current (SCLC) in Au/SnO2/n-Si Schottky diode with gamma-ray irradiation, J. Mater. Sci. Mater. Electron. 32 (2021) 15857–15863, https://doi.org/10.1007/S10854-021-06138-4.
[28] J.O. Bodunrin, D.A. Oeba, S.J. Moloi, Current-voltage characteristics of iron-implanted silicon based Schottky diodes, Mater. Sci. Semicond. Process. 123 (2021), 105524, https://doi.org/10.1016/J.MSSP.2020.105524.
[29] A. Afifi, A. Ayatollahi, F. Raissi, STDP implementation using memristive nanodevice in CMOS-Nano neuromorphic networks, IEICE Electron. Express 6 (2009) 148–153, https://doi.org/10.1587/ELEX.6.148.
[30] M.L. Litvak, C.J. Macdonald, B.L. Darlow, Validation and automatic tuning of integrated reservoir and surface pipeline network models, in: SPE Annual Technical Conference and Exhibition, Soc Pet Eng (SPE), Houston, TX, 1999, pp. 63–68, https://doi.org/10.2118/56621-MS.
[31] C. Antonio, Sequential model based optimization of partially defined functions under unknown constraints, J. Global Optim. 79 (2021) 281–303, https://doi.org/10.1007/S10898-019-00860-4.
[32] R.J. Dolan, Neuroscience and psychology: emotion, cognition, and behavior, Science 84 298 (2002) 1191–1194, https://doi.org/10.1126/SCIENCE.1076358.
[33] J. Delahunty, I. Verenikina, P. Jones, Socio-emotional connections: identity, belonging and learning in online interactions. A literature review, Technol. Pedagog. Educ. 23 (2014) 243–265, https://doi.org/10.1080/1475939X.2013.813405.
[34] Y. Wang, W. Song, W. Tao, A. Liotta, D. Yang, X. Li, S. Gao, Y. Sun, W. Ge, Wei Zhang, Wenqiang Zhang, A systematic review on affective computing: emotion models, databases, and recent advances, Inf. Fusion 83 (84) (2022) 19–52, https://doi.org/10.1016/J.INFFUS.2022.03.009.
[35] Z. Wang, X. Wang, A novel memristor-based circuit implementation of full-function pavlov associative memory accorded with biological feature, IEEE Trans. Circ. Syst. 65 (2018) 2210–2220, https://doi.org/10.1109/TCSI.2017.2780826.
[36] Z. Wang, X. Wang, Z. Lu, W. Wu, Z. Zeng, The design of memristive circuit for affective multi-associative learning, IEEE Trans Biomed Circuits Syst 14 (2020) 173–185, https://doi.org/10.1109/TBCAS.2019.2961569.
[37] Z. Wang, X. Wang, Z. Zeng, Memristive circuit design of brain-like emotional learning and generation, IEEE Trans Cybern. Early Access (2021).
[38] D. Ma, G. Wang, C. Han, Y. Shen, Y. Liang, A memristive neural network model with associative memory for modeling affections, IEEE Access 6 (2018) 61614–61622, https://doi.org/10.1109/ACCESS.2018.2875433.
[39] Z. Zhong, Z. Jiang, J. Huang, F. Gao, W. Hu, Y. Zhang, X. Chen, 'Stateful' threshold switching for neuromorphic learning, Nanoscale 14 (2022) 5010–5021, https://doi.org/10.1039/D1NR05502J.